Mitochondrial TFAM in the Regulation of FOXP3$^+$ T cell Mediated Maintenance of CD4$^+$ T Cell Landscapes

Kai Guo[1,2$], Trishna Debnath[3$], Zhihan Wang[4$], Shilpi Jain[3], Eden Abrham[3], Zachery Even[5], Het Mehta[3], Abby Lund[3], Mansib Rahman[3], Min Wu[2], Xusheng Wang[5], Junguk Hur[2], Adrian Ting[6], Holly Brown-Borg[2], Donald A Jurivich[3], Nadeem Khan[7], Ramkumar Mathur[3*]

1. Department of Neurology, University of Michigan, Ann Arbor, MI 48109, USA
2. Department of Biomedical Sciences, School of Medicine and Health Sciences, University of North Dakota, Grand Forks, ND 58202, USA
3. Department of Geriatrics, School of Medicine and Health Sciences, University of North Dakota, Grand Forks, ND 58202, USA
4. West China School of Basic Medical Sciences & Forensic Medicine, Sichuan University, Chengdu, Sichuan, China
5. Department of Biology, University of North Dakota, Grand Forks, ND 58202, USA
6. Department of Immunology, Mayo Clinic, Rochester, MN, USA
7. Dept of Oral Biology, College of Dentistry, University of Florida, Gainesville, FL, USA

[$]Authors contributed equally

***Correspondence**

Ramkumar Mathur, Department of Geriatrics, University of North Dakota, Grand Forks, ND, USA, 58203, Email: ramkumar.mathur@und.edu

Abstract: *The immune system deteriorates as we age. Regulatory T cells contribute to immunosenescence as they critically mold antigenic CD4$^+$ T cell subsets and maintain immunological homeostasis. Given the role of mitochondrial Transcription Factor A (TFAM) in oxidative stress, cellular senescence, and age-related pathologies, we explored the role of this factor in Regulatory T (Treg) cells. We employed a conditional deletion of FoxP3-specific TFAM to create Regulatory T (Treg) cells lacking mitochondrial TFAM. Using comprehensive single-cell RNA cell technology, we identified how mitochondrial TFAM in Treg cells controls the CD4$^+$ T cell fate and trajectory for a heterologous pool of inflammatory CD4 cytotoxic, CD4 exhausted, and CD4 effector memory T cells, all features of aging. Additionally, our results show how TNF signalling and related cell death pathways exacerbate systemic inflammation, degradation, and acceleration of cell death in mice lacking TFAM. Furthermore, partial TFAM restoration or use of the antioxidative drug resveratrol alleviate the inflammaging cascade. These findings reveal TFAM as a critical regulator of Foxp3 Treg cell activity in sculpting the CD4 heterologous pool and point to TFAM as a possible target for pharmacological manipulation in age-related diseases.*

The immune system is constantly reshaping due to everyday antigenic, metabolic, and epigenetic stresses (*1, 2*). Notably, Treg cells act as master regulators, preserving immune cell landscapes and reorganizing CD4 effector T cell responses to exert a distinct inflammation without jeopardizing the host (*3*). A decrease in peripheral Treg cells is considered to unleash effector CD4$^+$ T cells, which regulate inflammatory signals in a range of autoimmune and infectious diseases. While a significant increase in the number of Treg cells has been linked to increased organizing of inflammatory cytotoxic, exhausted, and effector memory T cells and a significant decrease in the pool of naive CD4$^+$ T cells as a conventional hallmark of aging T cells in aging animal models and humans. It is unclear if a residual pool of peripheral Tregs acquires a distinct immunosuppressive repertoire during thymic degeneration in aging and, as a result, influences the pool of effector cytotoxic, memory, and exhausted CD4$^+$ T cells. A range of age-related molecular and mouse genetic data is offered to explain the functional impairment of Tregs in inflammation control. Increased oxidative stress and cellular senescence have been linked to mitochondrial protein reduction in aging. In aging, the transcription factor TFAM (mitochondrial transcription factor A) has been linked to the regulation of effector T-cell responses (*4, 5*). Therefore, we hypothesized that TFAM in FOXP3 Tregs influences CD4-lineage distribution and affects aging CD4 landscapes. We leveraged a FoxP3-specific conditional TFAM deletion (Foxp3^{Cre}Tfam$^{f/f}$) and large-scale unsupervised single-cell RNA sequencing (scRNA-seq) approach to elucidate how TFAM expression in Tregs leads to the shaping of CD4$^+$ T cell cellular and functional heterogeneity.

To examine a comprehensive overview of how TFAM dysfunction influences cellular homeostasis in the spleen, we performed scRNA-seq from the whole splenocyte of Foxp3^{Cre}Tfam$^{f/f}$ (cKO) and Tfam$^{f/f}$ (WT). A total of 49,320 cells with 25 clusters were obtained from Foxp3^{Cre}Tfam$^{f/f}$ (cKO: 14,156) and controlled splenocyte Tfam$^{f/f}$ (WT: 35,164), and 21 cell types were identified (Erythroid cells were removed in the following analysis) in the spleen based on the canonical lineage-defining markers (Fig. 1A, B, Fig. S1A, S1C). Interestingly, we observed the absence of TFAM in Tregs led unrestrained inflammatory CD4 exhibiting increased inflammatory TNF signaling pathways and influenced overall induction of inflammation-driven aging and cancer pathways with TFAM lacking Treg mice (Fig. S1E). We found cKO cells largely exhibited marked upregulation of age-related genes, such as *S100a6*, *Zfp3612*, and influence decreased in longevity marker *Cd79b* and *Fcer2a* gene in bystander cell populations (Fig. S1D).

We further analyzed the CD4 cellular subsets and cellular heterogenicity, where sub-clustering of the 7,786 (WT: 4,133 and cKO: 3,653) CD4$^+$ T cells (CD4$^+$ T and CD4$^+$ Naïve T cells) revealed 12 clusters associated with six distinct CD4$^+$ T cell types based on the canonical markers: Naïve (*Sell*, *Lef1*,*Tcf7*, *Ccr7*), T effector memory (TEM: *S100a4*, *Lgals1*, *S100a10*), Exhausted (*Tnfsf8*, *Lag3*, *Tbc1d4*), normal Tregs (nTregs: *Ikzf2*, *Cd74*, *Il2ra*), aged Tregs (aTregs: *Icos*, *Rgs1*), and Cytotoxic cells (*Ccl5*, *Gzma*, *Gzmk*, *Eomes*) (Fig. 1C, 1D). We compared the relative changes of each subset in cKO versus WT mice, all cell populations, including aTregs, nTreg, TEM, Cytotoxic, Exhausted and Naïve cells (Fig. 1E, Fig. S2A). Surprisingly, we found both Tregs, aTregs (211.9%) and nTregs (7.2%) cells population markedly increased, while Naïve cells (-41.5%) population was significantly shrunken in the TFAM cKO compared to the WT mice. The TEM (125.1%), Cytotoxic (69.7%), and Exhausted (56.2%) cells were predominantly enriched in the TFAM cKO. We then examined the age-related DEGs and significant pathways among different CD4$^+$ T cells between cKO and WT mice (Fig. 1F and Fig. S2B). We found that inflammatory TNFa predominantly increases in Cytotoxic, Effector, and memory T cells (Fig. 1F). We found aTregs acquires inflammatory changes and were enriched with calcium signaling, cytokine, and chemokines signaling pathways, while they were markedly reduced the hematopoietic lineages turn over (Fig. 1F). Cytotoxic cell predominantly retains an increased inflammation and natural killer cell death and PDl1 and PD1 pathways involved in the cancer conditions. Increased IL17 signaling was found in the TEM and nTregs populations (Fig. 1F). Increased IL17 pathwayhas shown Tregs conversion to Th1 type Tregs. Overall, the induction of the inflammatory changes moderate Tregs immunosuppressive nature to inflammatory and age-related pathways.

To better understand the multilineage differentiation state and lineage relationships among these CD4$^+$ T cell clusters, we performed pseudo-time ordering analysis with WT and cKO cells together (Fig. 1G, Fig. S2C). Notably, we observed a differentiation trajectory with two bifurcation points indicating fate decisions and two primary differentiation paths (P1 and P2) with five Monocle states 1-5 (Fig. 1G, Fig. S2D). Parsing the Monocle states with WT and cKO CD4$^+$ T cells on the single-cell trajectory revealed that cells from the WT mainly converged on states 4 and 3, while cells from cKO converged more on states 1, 4, and 2 (Fig. 1G, Fig. S2D). We also compared the cells occupied in these different states among WT and cKO (Fig. S2E), which revealed that state 4 mainly consists of the naïve cells in both the WT and cKO groups. Additionally, the exhausted cells were increased in cKO while TEM cells were decreased in state 1(Fig. S2E). These findings suggested that the CD4$^+$ T cell from WT mainly follows a cell fate trajectory (P1), and cells from cKO instead had a preferred lineage bias toward state 1 (P2) (Fig. 1G). To further verify the directionality in the pseudo-time trajectory, we performed RNA velocity analysis to estimate the expression of unspliced and spliced mRNAs in the trajectory (Fig. 1I, Fig. S2G). The RNA velocity analysis also showed a clear directional flow at the end of each branch point, further corroborating the Monocle analysis (Fig. 1G). However, it is also worth noting that some RNA velocity vectors do not follow specific trajectories.

We then checked the enriched KEGG pathways related to each state by using Gene Set Enrichment Analysis (GSEA). Interestingly, we found a distinct decrease in the hematopoietic pathways essential to cell renewal and homeostasis. Decreased antigen presentation and processing results in defective proteostasis and defects in clearance of accumulated proteins, which reflect age-related disease pathways such as Alzheimer disease, ALS, and Parkinson disease exhibited a significant increase in state 1 (Fig. S2F). To reveal the sequential gene expression dynamics along each branch, we also visualized the gene expression dynamics along the pseudo-time trajectory and observed four distinct clusters according to their expression pattern (Fig. 1H). Genes in cluster 1, such as *Klf3*, *Sell*, *Bcl2*, and *Satb1*, were highly expressed in the early stages of the differentiation process. Genes in cluster 2 were highly expressed in the terminally differentiated cells such as *Anxa2*, *S100a4*, *Ccl5*, *S100a6,* and *Lgals1*. Functional enrichment analysis of the four clusters revealed that cluster 1 was a highly enriched hematopoietic pathway. Cluster 2 was enriched in Parkinson disease, Amyotrophic lateral sclerosis, Alzheimer disease, and Oxidative phosphorylation pathways (Fig. 1H). Since our primary interest was in the

differentiation of cKO $CD4^+$ T cells, we also identified the putative driver genes by using their likelihoods. The dynamic expression of the top 50 highest likelihood-ranked genes associated with $CD4^+$ T cell differentiation were shown in Fig. S2G. Genes such as *Klf3*, *Sell*, *Bcl2,* and *Satb1* were highly expressed in early differentiation stages, while *Anxa2*, *S100a4*, and *S100a6* genes were mainly expressed in ending stages. Notably, the homeostasis of $CD4^+$ T memory cells is more dynamic than that of naïve T cells. We discovered a significant increase in the effector memory $CD4^+CD44^{hi}CD62L^{low}$ population and a decrease in the naive $CD4^+CD44^{low}CD62L^{hi}$ population (Fig. 1J, 1K). Further work demonstrated that in TFAM cKO mice, $CD44^{hi}CD62L^{low}$ (T effector/effector memory, TE/EM) expression is more common in $CD4^+$ T cells (Fig. 1K). Tregs from TFAM cKO mice displayed lower suppressive ability when employed in in vitro T cell suppression experiments with incubated $CD4^+$ T effector cells, suggesting that TFAM loss affects Treg functional ability and, as a consequence, CD4 population reconstruction (Fig. 1L).

Notably, TFAM ablated CD4 cells showed cellular senescence, and mice exhibited age-related symptoms (*6*). We further evaluated TFAM function for $CD4^+$ Tregs and cellular and molecular evidence linked to physiological and survival alterations in mice. Indeed, TFAM deficiency was much more sensitive in *Foxp3* cell , and as a consequence of the immunological shift, the cKO mice exhibited severe physically impaired and slow movement. Interestingly, pups were born with normal mendelian ratios. After four weeks, cKO mice started to lose hair (alopecia), shrink in size, develop lymphadenopathy, show evidence of kyphosis on X-ray imaging, and showed progressively lethargic behavior as well as a significantly shorter life span ($p=0.0001$) due to TFAM depletion (Fig. 2A-2D). The histopathological analysis at 8–10 weeks confirmed the shrunken thymus, muscle destruction, reduction of fat cells in the skin, and decreased bone thickness (Fig. 2E, 2F). We also observed the infiltrated inflammation among the spleen, lung, liver, and kidney (Fig. S3A). Furthermore, cKO mice have lost their spleen marginal zone (Fig. 2H) and demonstrated a systemic inflammatory index with elevated TNFα, IL-6, IFNγ, and serum cytokines (Fig. 2G, Fig. S3B), indicating that the Tregs were impaired in controlling systemic inflammation, and this resulted in deteriorated immune function at different tissue locations when compared to WT mice (Fig. 2G). Compared to WT mice, the mitochondrial potential in cKO mice, assessed by Mitospy in splenocyte by IHC and FACS, was lower (Fig 2H, 2I). qPCR analysis demonstrated an age-related rise in the expression of p16 and p21 in the spleen of cKO mice (Fig. 2J). Western blot analysis indicated that cKO mice expressed more CDK4, PCNA, p53, p16, and p21 proteins than control mice (Fig. 2K). Bulk RNA sequencing of the spleen showed several alterations leading to the expression of age-related genes (Fig. 2L). GSEA results of RNAseq from multiple organs showed that cKO mice exhibited age-related and abnormal responses, including increased brain neuroactive ligand-receptor pathways, decreased splenic protein export, and abnormal skin clock rhythm pathways (Fig. 2M).

Because the combined activity of TFs is mainly responsible for the regulation of $CD4^+$ T cell identification and function (*7-9*), we examined the specific set of regulons that appear to be active within the identified subsets. A total of 173 high-confidence regulons were identified (Fig. 3A). The regulons such as *Irf2*, *Pml*, *Bcl11a*, *Irf8* were primarily active in WT cells, and the *Batf*, *Rora*, *Maf*, and *Runx2* were mainly active in cKO cells (Fig. 3A, Fig. S4). The three regulons, *Chd2*, *Ahr,* and *Gata3,* displayed high activity in aTregs, Exhausted and nTregs cells in cKO mice (Fig. 3A). Some regulons such as *Foxj3*, *Foxj2*, *Ddit3,* and *Runx3* were active among all cells across WT and cKO (Fig. 3A). We then checked the expression of the inflammaging genes, such as *Prdm1*, *Nfkb1*, *Nfkb2* and *Ahr*, among all $CD4^+$ T cells between WT and cKO (Fig. 3B). All these genes were up-regulated in cKO cells, especially in Tregs cells. In accordance with the excessive systemic inflammatory cytokine such as TNFα, IL1β and IL6 response observed in TFAM cKO mice (Fig. 3C), we next investigated whether Foxp3 T regs contribute to increasing inflammatory responses and encouraging bystander cell death pathways in these mice. Notably, scRNA-seq data suggests an increase in the inflammatory CD8 and NK cell populations, as well as the B cell population (Fig. 1A, S1B). In contrast, when comparing cKO mice to WT mice, the number of naive CDT cells and naive B cells significantly decreased (Fig. 1A, Fig. S1B). Increased TNFa responsive signaling in CD4, CD8 and B cell types is associated with TFAM dysfunction in Foxp3 T regs (Fig. S1E). Inflammatory signals have been shown to cause a decrease in mitochondrial membrane potential as well as the onset of cell death signals (*10-13*) . Unbiased bulk RNA sequencing results also showed that cKO animals had higher levels of necroptosis and apoptosis than WT mice (Fig. 3D). Increased cell death is further confirmed by a western blot for the detection of necroptosis induced by the activation of the RIPK1, RIPK3, and MKLK proteins, as well as by other methods (Fig. 3E). Increased Annexin /PI cell death was observed in the spleen and skin tissue of cKO mice, consistent with the low mitochondrial potential and inflammatory environment found in cKO mice (Fig. 3F). These findings indicate that excessive inflammatory, caused by impaired Treg function, result in excessive inflammation and cell death in various tissues.

Our data indicate that senescent T regs had a detrimental effect on the makeup of $CD4^+$ T cell subsets. We then tested resveratrol (RSV), a naturally occurring phenolic compound that has been identified as a potential antioxidant candidate capable of improving mitochondrial function by suppressing oxidative stress and inhibiting the inflammatory response in the laboratory setting *(14, 15)*. TFAM cKO mice were treated with resveratrol (hereinafter; RSV+) for three weeks (7mg/kg/day) and then compared to untreated TFAM cKO mice to see which group performed better (hereinafter; RSV-) (Fig. 4A). In RSV+ mice, RSV therapy increased the mitochondrial membrane potential in the skin, protecting mice from histological damage and preserving their health (Fig. 4B, Fig. S5A). We found that the expression of IL1a, IL6, and cytokines was reduced compared to RSV-animals after the study period (Fig 4C, 4F). When comparing RSV+ mice to RSV-mice, we discovered that age-related p16 and p21 expression in the splenocytes of RSV+ and RSV-mice were considerably lower in the RSV+ mice (Fig. 4D, 4E). Overall, our data imply that RSV therapy may decrease systemic inflammation and immunological aging. However, more study is necessary to understand the molecular mechanisms of action in greater detail. Because the expression of TFAM declines with aging in elderly people. In older individuals, this essential fact is supported by our TFAM ablated $Foxp3^{Cre}Tfam^{f/f}$ mouse's short lifespan. Interestingly, 50% partial restoration of TFAM activity in $Foxp3^{Cre}TFAM^{f/+}$ (TFAM Het mice) establishes mechanistically the TFAM-mediated regulation of the inflammatory response in Treg/$CD4^+$ T cells. We found that TFAM Het mice displayed delayed immunological aging pathology at about 30-32 weeks of age, including hunchback posture and progressive weight loss, impaired breeding, elevated levels of pro-inflammatory TNFα, IL6, and IL1 cytokines, and increased age-related p16 and p21, p53, and CDK4 expression levels (Fig 4G-I).

In summary, our data indicate that Foxp3 Tregs are essential for maintaining a homeostatic CD4 T cell subset. The role of mitochondrial proteins in oxidative stress and cellular senescence has been well documented. The mitochondrial protein TFAM has recently been shown to alter the immune cell homeostasis and stability of Foxp3Treg cells in the tumor microenvironment (*16-18*) . Recent research revealed that mitochondrial TFAM has been implicated in the regulation of adaptive T-cell responses (*6*). Since the depletion of CD4 Foxp3 Tregs has been shown to increase cellular senescence and the risk of age-related physical, metabolic, and cognitive impairment resulting in premature death, we asked that depletion of TFAM in Foxp3 Tregs, a subtype of $CD4^+$ T cell, would enable in narrowing the basis for CD4 T cell-driven aging-related pathologies. Indeed, as anticipated, the loss of TFAM in Foxp3 cell mice were much more sensitive and $Foxp3^{Cre}Tfam^{f/f}$ mice exhibits effective sign of physical, and cognitive impairment and shortened life span. Given that a heterogeneous $CD4^+$ T cell pool in old mice demonstrates an aging phenotype, studying CD4 heterogeneity throughout aging is critical. The inability to access previously reported $CD4^+$ T cell subset markers, as well as the use of a limited number of cells, which may obscure complex CD4 cellular compositions, are the major constraints of using conventional flow cytometry techniques. This is the first work employing scRNA-seq to reveal that TFAM is required for Treg homeostasis and that its dysregulation in FOXP3 T regs leads to alterations in CD4 complex composition and age-related effector $CD4^+$ T cell activity. Foxp3-expressing $CD4^+$ T cells are required for the conversion of non-regulatory T cells (NRTs) to regulatory T cells (Tregs) in order to maintain homeostatic proliferation during aged thymic involution. Increased peripheral inflammation reduced FOPX3 expression, and Tregs can be transformed into T helper cells like Th1 and Th17 (*13, 19*) , while others think Tregs are resistant to this plasticity due to their prolonged lifespan (*20*). Inflammatory phenotypes and Treg diversity are critical for sustaining chronic inflammation and the inflammatory-induced aging process. Notably, inhibiting the FoxP3-specific TFAM results in a population imbalance favoring inflammatory aTreg and cytotoxic effector T cells. Furthermore, findings from the spleen's whole single-cell landscape indicate an increase in inflammatory CD8 and NK cell populations, which leads to extended TNFa receptor activation, downstream programmed cell apoptosis, and necroptosis cell death. The inability of TFAM without Tregs to respond to TNFa was increased in the spleen, lung, colon, and skin tissue of TAFM cKO mice, together with a wide distribution of Tregs and CD4+ T cells. As a consequence, systemic inflammation develops, and the mice die at a greater rate than control animals. A better understanding of how TFAM maintains Treg homeostasis might benefit in the development of anti-inflammatory drugs capable of preventing cell death.. Our data suggest that pharmaceutical antioxidant resveratrol or partial TFAM retention ameliorates the diseases caused by Tfam ablation in Tregs. Thus, our results provide a new justification for the use of targeted mitochondrial TFAM regulation, specifically targeting Foxp3 Tregs, in the therapy of age-related pathologies.

Materials and Methods.

Animals. Foxp3^{YFPCre} (Stock No: 016959) and TFAM$^{f/f}$ (Stock No: 026123) mice were obtained from Jackson Laboratory (Bar Harbor, ME) and bred at the UND animal facility to create FOXp3^{Cre}TFAM$^{f/f}$. All mice were C57/BL6. All animals were kept and bred in the UND Animal facility in a pathogen-free unit with a 12-hour light cycle (lights on at 7:00 a.m.), as well as temperature and humidity control. Efforts are being made to reduce animal suffering and needless usage, in accordance with the Institutional Animal Care and Use Committee's (IACUC) and National Institutes of Health's Guide for the Care and Use of Laboratory Animals standards.

Histology, Immunohistochemistry, and Acquisition of Images. Formalin-fixed, paraffin-embedded slices of various tissues were deparaffinized on slides using xylene twice for 5 minutes each. Following that, they were transferred to 100 percent ethanol twice for 3 minutes each and then to 95 percent, 75 percent, 65 percent, 50 percent, 35 percent, and 25% ethanol for 3 minutes each. The slides were then rinsed for ten minutes under running tap water. The excess water was removed using a wiper (KIMTECH, SCIENCE* BRAND) and 100 l of 10% fetal bovine serum (FBS) in PBS was applied to the sections of the slides and incubated for 30 minutes in the dark at room temperature (RT). FBS was gently drained from the slides and cleaned with PBS (1X). MitoSpy (excitation (ex)/emission (em) at 577 nm/598 nm, mitoSpyTM Red CMXros Cat# 424801, BioLegends). After incubation, slides were washed twice with 1X PBS and a single drop of mounting media (Fluromount-GTM, with DAPI, CAT-00-4958-02, Thermo Fisher Scientific) was applied to the tissue sections and the coverslip was dipped into the mounting solution. All pictures were collected using an Olympus TIF Fluorescence microscope equipped with a Hamamatsu ORCA-Flash4.0 camera.

Western Blot. Proteins were isolated from mouse tissue and/or single cells and homogenized in RIPA lysis buffer containing a 1% protease inhibitor cocktail (*21-23*). The protein concentration was determined according to the manufacturer's instructions and our previously published protocol using the Bio-Rad protein assay reagent. SDS-PAGE was used to extract a set quantity of cellular protein and electroblotted onto an Immobilon-P transfer membrane (cat# IPVH00010). The immunological blot was blocked for 1 hour at room temperature with 5% nonfat dry milk in TBST (25 mM Tris–HCl, pH 7.4, 1.5 M NaCl, 0.05 percent Tween-20), followed by overnight incubation with primary antibodies at 4C. The next day, the membranes were washed five times at six-minute intervals and incubated for one hour with HRP-conjugated secondary antibody (A16172, Invitrogen) (1:1000) in 3% nonfat dry milk in TBST. The blots were then washed five additional times with TBST and developed with enhanced chemiluminescence. The following primary antibodies were bought from Cell Signaling Technologies (Cell Signaling Technology, MA 01923, USA): REMEMBER (D94C12) MLKL Rabbit mAb #3493, XP® (D2I6N) RIP3 rabbit monoclonal antibody #14993 (E1Z1D) p-RIP rabbit monoclonal antibody #13526 (S166) p-RIP3 rabbit monoclonal antibody #65746 (S227) p-MLKL rabbit monoclonal antibody #93654 (S358) #91689 rabbit monoclonal antibody to p21 Waf1/Cip1 (12D1) p53 rabbit monoclonal antibody #2947 (1C12) Mouse monoclonal antibody #2524, CDK4 (D9G3E) Rabbit monoclonal antibody #12790, PCNA (D3H8P) XP® Rabbit monoclonal antibody #13110, p16 INK4A (D3W8G) GAPDH (D16H11) XP® Rabbit mAb #5174.

RNA Isolation, and qPCR. Total RNA was isolated from mouse tissues or single cells cultured in the presence of CCCP or TNF+zvad. The tissues were shredded with a scissor and added to 500L of TRIzol reagent (ambion, cat# 15596018, Life technologies, USA) (*21-23*). A Fisher Scientific Sonic Dismembrator 100 was used to fully homogenize tissue solutions (American Laboratory Trading, East Lyme, CT 06333. USA). The upper layer was removed, and the RNA was precipitated with an equivalent volume of isopropanol and incubated at 55 °C for 10 minutes before being resuspended in 50 l of RNase-free water (Promega, Madison, WI, USA). We determined the concentrations of RNA using a Smart-Spec plus spectrophotometer (Bio-Rad). Then, using a High-Capacity cDNA Reverse Transcription Kit (Cat#: 4368814, Applied Biosystem, Thermo Fisher Scientific), cDNA was generated from 0.5-1 g of total RNA in a total volume of 25 l. The RT-PCR program was run for 5 minutes at 25 °C, 30 minutes at 42 °C, and 30 minutes at 95 °C. The cDNA templates were further diluted in water two-three times. For qPCR, two microliters of diluted templates were utilized. A 96-well PCR plate (Cat#MLL9601, Bio-Rad) was used for the qPCR. All genes were amplified twice and each sample was analyzed in triplicate using 2X SYBR Green dye (Cat#: B21202, Bimake.com). After normalization to GAPDH, the CT value was utilized to compute the fold change in RNA abundance. qPCR reactions were performed using the Aria Mx Real-Time PCR equipment (Agilent). Supplementary Table 1 contains the primer sequences for all primers.

Flowcytometry. Single-cell suspensions were prepared from mouse tissues or blood serum. Centrifuged at 3000rpm/7min/RT for 7 minutes and discarded the top layer. The cells were then resuspended in 50 ml FACS buffer (1 percent BSA, 2 mM EDTA, and 0.1 percent sodium azide in PBS, pH 7.4) (5–10 105 cells/tube) and incubated for 30 minutes at 37°C with Mitospy according to the manufacturer's instructions. Centrifuged (1 cc of warm 1XPBS twice) at 5000 rpm for 3 minutes at room temperature. Resuspended stained cells in 300-400 ul

of ice-cold Facs buffer and immediately examined stained and unstained samples using a BD FACSymphony Flow Cytometer (BD Biosciences).

Sequencing library construction using the 10x Genomics Chromium platform

The 10x Genomics Chromium system was used to create 3' single-cell gene expression libraries (v3.0) from WT and KO spleen single-cell suspensions. On an Illumina HiSeq X Ten, pair-end 150 bp sequencing was used to generate high-quantity data (Illumina, San Diego, California, USA). Then, using Cell Ranger software v4.0.0, the output Illumina base call files from sequencing runs were combined and converted to FASTQ files using Illumina's bcl2fastq.

Single-cell RNA-seq data alignment and sample aggregating

RNA reads from the 10X Chromium platform with sequence quality less than 30 were filtered out and then mapped to the GRCm38 mouse reference genome using the CellRanger software (version 4.0.0). Seurat v4 was used to read the individual sample output files from CellRanger Count (*24*). Cells were further filtered out for the downstream analysis using the following criteria: UMI counts per cell, gene counts per cell, and the proportion of transcripts mapped to mitochondrial genes (*nFeature RNA > 200 & nFeature RNA > 4000 & percent.mt <1,* respectively). To detect probable doublets in the data, we used Scrublet (*25*), which calculates the chance that a cell is a doublet using barcode and UMI information. Then, we utilized the Seurat function *CellCycleScoring* to define cell cycle phase and compute G1/S and G2/M phase scores for each cell using a published list of cell cycle genes (*26*). *SCTransform* from Seurat was used to independently normalize the gene-cell count matrices, with the "*vars.to.regress*" parameter set to the proportion of mitochondrial genes, cell cycle score, and default values for other parameters (*27*). Finally, the datasets were integrated using the Seurat *SCTransform* integration workflow.

Dimension reduction, clustering, and visualization

To identify cell clusters, we first performed principal component analysis ("*RunPCA*" function) on the list of highly variable genes. The top 30 PCs were used for clustering with the Louvain modularity-based community detection algorithm to generate cell clusters (*FindClusters* function, *resolution = 0.4*). We finalized the resolution parameter on the *FindClusters* function once the cluster numbers didn't increase when we increased the resolution. We then performed the t-distributed Stochastic Neighbor Embedding (t-SNE) projections to present high dimensional data into two-dimensional space, the first 30 PCs were used via *RunTSNE* function using the default setting. By following a similar pipeline, subclusters for $CD4^+$ T cells were identified.

Cell type annotation and differential expression analysis

To determine the cell type of each cluster, the *FindAllMarkers* function in Seurat was used to find the cluster's gene markers. Cell types were allocated manually after consulting the CellMarker and PanglaoDB databases. Cluster reassignment was conducted manually based on the expression of lineage-specific markers. MAST was utilized to conduct differential analysis on each cell type to find the genes that were differentially expressed between WT and cKO cells. If the corrected P-value was less than 0.05 and the average log2FC value was more than 0.25 or less than -0.25, the genes were declared differentially expressed. The Kyoto Encyclopedia of Genes and Genomes (KEGG) Gene Set Enrichment Analysis (GSEA) was done using the richR package (https://github.com/hurlab/richR), with an adjusted P-value of 0.05 used as the cutoff value to identify significant KEGG.

Single-Cell Trajectory Reconstruction for $CD4^+$ T cell

The Monocle2 R package (version 2.8.0, http://cole-trapnell-lab.github.io/monocle-release/) was used to reconstruct cell fate choices and pseudotime trajectories. The gene-cell matrix in the scale of UMI counts was sent to Monocle, which then created an object using its new Cell Data Set function (*lower Detection Limit = 0.1, expression Family = nonbinomial.size*). We evaluated the size factors and dispersion of gene expression. We next used the differentialGeneTest module to conduct differential expression analysis to determine the ordering of genes using the parameter "*fullModelFormulaStr = ~celltype*," and then maintained genes with q values less than 0.01 for downstream analysis. Following the *setOrderingFilter* function, the *reduceDimension* module with the argument "*method = DDRTree*" was used to reduce the dimensionality of the data. When *orderCells* is executed, the root state variable may be adjusted to reflect the known biological background. Following that, the

plot cell trajectory, plot genes in pseudotime, and plot genes branched heatmap functions were used to visualize the data further.

RNA velocity analysis

Velocyto was used to analyze the velocity of RNA in cells (*28*). This method utilizes the relative amount of unspliced and spliced mRNA as a predictor of future cell state. Annotation of spliced and unspliced reads was conducted using the Python script velocyto.py in the Cell Ranger output folder utilizing the velocyto pipeline. Then, the scvelo (*29*) was used to determine the $CD4^+$ T cell velocity. The previously normalized data served as the basis for calculating first and then order moments for each cell in relation to its closest neighbors (*scvelo.pp.moments(n pcs = 30, n neighbors = 30)*). Following that, the velocities were calculated, and the velocity graph was produced using the *scvelo.tl.velocity* and *scvelo.tl.velocity* graph functions with the mode set to 'stochastic'. Finally, using the *scvelo.tl.velocity* embedding function, the velocity field was projected onto the existing t-SNE coordinates.

Transcription factor regulons prediction

Gene regulatory network (GRN) was generated using pyscenic package (*30*). Briefly, the raw expression matrix for the cells of all samples was filtered by keeping genes with a total expression greater than 3*0.01*(number of cell). Then the *pyscenic.grn* command was used with *grnboost2* method and default options and a fixed seed to derive co-expression modules between transcription factors and potential targets. The following database: cisTarget databases (*mm10__refseq-r80__10kb_up_and_down_tss.mc9nr.feather, mm10__refseq-r80__500bp_up_and_100bp_down_tss.mc9nr.feather*), the transcription factor motif annotation database (*motifs-v9-nr.mgi-m0.001-o0.0.tbl*) and the list of mouse transcription factors (*mm_mgi_tfs.txt*)were downloaded for the analysis. A regulon is a group of target genes regulated by a common transcription factor. AUCell (Area Under the Curve) scores (regulon activities) in each cell were computed with *pycenic.aucell* command (default paramaters). These scores were then binarized into either “on” or “off” states, by setting an optimized threshold on the distribution of each regulon among all cells using the *skimage.filters.threshold_minimum* function.

RNA-seq data processing

Low quality (Q<30) and sequencing adapters were removed with Trimmomatic software v0.36 (*31*) from raw reads. Clean reads were then mapped to the mouse reference genome (mm10) by using HISAT2 (*32*). FeatureCounts (*33*) were used to summarize the unique mapped reads to mouse genes. Differential gene expression analysis was performed using DESeq2 (*34*) with adjusted p-value < 0.05 and fold change >2 as the cutoff for differentially expressed genes (DEGs) identification. Gene Set Enrichment Analysis (GSEA) for KEGG was performed by using the richR package and the adjusted P-value < 0.05 was chosen as the cutoff value to select significant KEGG.

Acknowledgments

We thank the Epigenetic core, Flow cytometry core, Histology core, and Computational Data Analysis core at the University of North Dakota.

Funding: R.M. is supported by UND NIH HOST PATHOGEN COBRE PILOT Grant (grant no. NIGMS/NIH-P20GM1034442) and the S.J. is supported by UND NIH Epigenetic COBRE Pilot Grant. Histological services provided by the UND Histology Core Facility are supported by NIH/NIGMS awards P20GM113123, U54GM128729, and UND SMHS funds. Computational Data Analysis core was supported by NIH/NIGMS award P20GM113123.

Author contributions: R.M. conceived and designed the study, K.G, R.M., and Z.W. analyzed and interpreted the scRNA-seq and RNAseq data, T.D., H.M., A.L., and S.J. performed the experiments. R.M., K.G., N.K. and Z.W. organized the figures and wrote the manuscript. R.M., K.G., N.K., J.H., Z.W., and A.L. revised the manuscript. All authors provided comments on the manuscript.

Competing interests: The authors declare no competing interests.

Data and materials availability: All data associated with this study are present in the paper or the Supplementary Materials.

Figure Legends:

Figure 1: TFAM in FOXP3 Tregs role as a determinant of CD4-lineage distribution and to regulate immune-mediated aging.

A. schematic representation of the scRNA sequence.

B. t-SNE projection of 49,320 cells with 21 cell types (Erythroid cells were removed) were obtained from Foxp3^{Cre}Tfam$^{f/f}$ (cKO: 14,156) and controlled splenocyte Tfam$^{f/f}$ (WT: 35,164). Colors represent for different cell types.

C. t-SNE projection of all 7,786 cells (WT: 4,133; cKO: 3,653) of CD4^{+} T cells presenting six different CD4^{+} T cells (Naïve, TEM, Exhausted, nTregs, aTregs and Cytotoxic cells). Colors indicate different cell types.

D. Heatmap of gene expression profile across cells. All CD4^{+} T cells were grouped by subset and groups (horizontal bars). Genes shown were up-regulated significantly [log2(fold change) > 0.25, adjusted P < 0.05] in at least one subset compared to all other cells. Genes were ordered by significance and associated with the subset with higher detection rates.

E. Relative changes of six types of CD4^{+} T cell between cKO and WT spleen.

F. GSEA for KEGG pathways for CD4^{+} T cells between cKO and WT. Color stands for the up-regulated (red) or down-regulated (blue) in cKO spleen.

G. Pseudo time map of the CD4^{+} T cells reflects the developing relationships and reveals potential paths of the CD4^{+} T subtypes in WT and cKO. Each dot represents one cell and color stands for different cell type.

H. Expression pattern for the expression of the 2,397 ordering genes. Cells were ordered in pseudotime; columns represent cells, rows representing genes were grouped based on similarity in gene expression, resulting in four clusters, with genes in clusters 1 expressed early in pseudotime, and genes in cluster 2 expressed late. KEGG enrichment analyses were performed for genes in each cluster, with selected significantly enriched pathways shown.

I. Velocities derived from the dynamical model for CD4^{+} T cells are visualized as streamlines in a t-SNE-based embedding.

J. CD4^{+}CD44^{hi}CD62^{lo} CD4 effector and CD4^{+}CD44^{lo}CD62^{hi} CD4 naïve T cell from WT and cKO detected by FACS, and **K.** mean fluorescence intensity (MFI) plot from different organs. CD4^{+} T effector T cell number greatly increased in lung, skin, and colon of the cKO mice compared to the WT mice.

L. T cell suppression assay for CFSE labeled CD4^{+} Tconv cells co-cultured with Tregs in indicated ratio for 60 hours in the presence of CD3/CD28 stimulated or non-stimulated Tconv cell CFSE proliferation detected by FACS Symphony, data analyzed by FlowJo, plotted as percent suppression.

Figure 2: TFAM ablation exhibits systemic pathology and accelerates immune aging in Foxp3^{YFPCre}Tfam$^{f/f}$ mice.

A. Representative photograph from cKO mouse(right) exhibits deteriorated appearance compared to the same age (8week) and sex littermate WT mouse(left).

B. Increased spleen and lymph node size in cKO mouse compared to WT mice.

C. cKO mouse(right) shows increased spine curvature compared to the same age (8week) and sex littermate WT mouse(left) showing by representative X Ray image.

D. Kaplan Meir survival curve for WT (n=10; M/F) and cKO mice (n=10, M/F).

E. Histology sections stained by H&E from bone, muscle and skin and images were taken by light microscope, and **F.** quantification of muscle and bone density plotted.

G. Serum cytokines from for TNFα and IL6 were detected by Legend plex, and calculated values were plotted

H. H&E and Mitospy staining in spleen section form cKO mouse compared to WT mice.

I. Mitospy staining from WT and cKO splenocytes, detected by FACS and plotted as a histogram.

J. p16 and p21 aging marker from mouse spleen detected by quantitative PCR and plotted.

K. Protein expression of aging markers including, CDK4, PCNA, p53, p21, p16, LC3B and GAPDH detected by western blot

L. Differential expression genes expression profiling between WT and cKO in the spleen.
M. Bulk RNA Seq expression from cKO mice compared to the WT mouse showing reduced protein and N-Glycan biosynthesis pathways in spleen and reduced circadian rhythm in the skin, increased neuroactive ligand receptor signaling in the brain and of cKO mice.
Data represented as mean ± SEM t-test. $^{*}p < 0.05$, $^{**}p < 0.01$, and $^{***}p < 0.0001$, WT (n=5-10; M/F) and cKO mice (n=5-10, M/F).

Figure 3. Predominance of inflammatory and cell death pathways in TFAM cKO mice
A. Heatmap of all $CD4^{+}$ T cells showing the high-confidence regulons among WT and cKO mice. "On" indicates active regulons; "Off" indicates inactive regulons. Active regulons per cell appear in black; the horizontal color bar indicates the subset associated with each cell and group. Numbers in parentheses represent the number of genes comprising the regulon.
B. Dotplot showed the expression of *Prdm1*, *Nfkb1*, *Nfkb2* and *Ahr* between WT and cKO among all $CD4^{+}$ T cells.
C. Inflammatory *TNFα*, *IL1β*, and *IL6* cytokines expression detected by qPCR from WT and cKO spleen.
D. Heatmap showed the apoptosis and necroptosis expression profiling between WT and cKO in the spleen.
E. Protein expression of TNF downstream pRIPK1/RIPK1, pRIPK3/RIPK3, pMLKL/MLKL and GAPDH as loading control detected by western blot.
F. Annexin V staining for live and dead cell from spleen and skin detected by flowcytometry in WT and cKO mice.
Data represented as mean ± SEM t-test. $^{*}p < 0.05$, $^{**}p < 0.01$, and $^{***}p < 0.0001$, WT (n=5-10; M/F) and cKO mice (n=5-10, M/F).

Figure 4. The restoration of TFAM function results to alleviate inflammation and aging pathologies.
A. Schematics for resveratrol (RSV) treatment for cKO mice.
B. Skin histological sections stained for H&E and Mitospy from vehicle and resveratrol treated cKO mice
C. TNFα and IL6 serum cytokines from TFAM cKO mice.
D. *p16* and *p21* expression detected by western blot, and **E.** qPCR from vehicle and resveratrol treated cKO mice.
F. Proinflammatory *IL1β*, *Il6*, and *TNFα* cytokine expression detected by qPCR from vehicle and resveratrol treated cKO mice.
G. Representative photograph from TFAM Het ($Foxp3^{YFPCre}Tfam^{f/+}$) mouse showing an aging appearance compared to the same age (8 months) and sex littermate control $Tfam^{f/f}$ mouse(left).
H. Protein expression of aging markers including p16, p21, and GAPDH detected by western blot.
I. TNFα and IL6 cytokine detected from serum from 8 week and 8 months of WT and cKO mice. **J.** Representative working model.
Data represented as mean ± SEM t-test. $^{*}p < 0.05$, $^{**}p < 0.01$, and $^{***}p < 0.0001$, WT (n=5-10; M/F) and cKO mice (n=5-10, M/F).

Supplementary Materials
Supplementary Figure 1. Landscape of scRNA-seq analysis of WT and cKO spleen.
A. t-SNE projections of single-cell transcriptomes from WT and cKO mice before Erythroid cells were removed, annotated by cell type. Each dot denotes a distinct cell.
B. Cell subset proportions for WT and cKO spleens.
C. Dot plot of mean expression of canonical marker genes for 20 major lineages from tissues of each origin, as indicated.
D. Expression of aged-related genes (*Fcer2a*, *Cd79b*, *Zfp36l2*, and *S100a6*) on Figure 1 t-SNE embedding. Each dot corresponds to a single cell.
E. Gene Set Enrichment Analysis (GSEA) of KEGG pathways for all cell types between cKO and WT (Only age-related pathways are selected). Color stands for the up-regulated (red) or down-regulated (blue) in cKO spleen. Enriched terms were identified as significant at an adjusted P value ≤ 0.05.

Supplementary Figure 2. scRNA-seq results show the cellular heterogeneity in CD4+ T cells.
A. Relative proportion of $CD4^{+}$ T cells among WT and cKO spleen, color stands for cell type.

B. Heatmaps show the expression profile of age-related genes among all $CD4^+$ T cells. Only the significant differential expression genes between cKO and WT spleen in at least one of these six types of $CD4^+$ T cells were selected.
C. Monocle 2 prediction of CD4+ T cell subsets developmental trajectory with pseudotime. Each dot represents a single cell.
D. Relative proportion of $CD4^+$ T cells among different states of WT and cKO spleen, color stands for cell type.
E. Differentiation trajectory generated with all $CD4^+$ T cells, each branch represents one cell state. (right). Barplots representing cell proportions in the five states of WT and cKO (left). Cells are colored according to five states, which partition the trajectory.
F. Gene Set Enrichment Analysis (GSEA) of KEGG pathways for the five cell states.
G. Gene expression dynamics resolved along latent time shows a clear cascade of transcription in the top 50 likelihood-ranked genes.

Supplementary Figure 3. Increased cell infiltration and inflammation in different organs in Foxp3 Tfam$^{f/f}$ mice.
A. Histology sections stained with H&E from lung, liver, colon, and kidney.
B. Serum cytokines identified by Legend plex for TNFα, IL1β, IL6, IL10, MCP1, IL23, Il1α, IL17, IFNγ, and IL12, IFNβ, GM-CSF and IL27 with estimated values displayed.
Data represented as mean ± SEM t-test. $^*p < 0.05$, $^{**}p < 0.01$, and $^{***}p < 0.0001$, WT (n=5-10; M/F) and cKO mice (n=5-10, M/F).

Supplementary Figure 4. t-SNE projection of average binary regulon activity of *Foxo1*, *Eomes*, *Bcl11a*, and *Irf8* that were cell type and group-specific in $CD4^+$ T cells.
Supplementary Figure 5. H&E histology section for lung, liver, and kidney for RSV treated WT and cKO mice**.**

References

1. C. Franceschi, A. Cossarizza, Introduction: the reshaping of the immune system with age. *Int Rev Immunol* **12**, 1-4 (1995).
2. J. J. Goronzy, C. M. Weyand, Successful and Maladaptive T Cell Aging. *Immunity* **46**, 364-378 (2017).
3. Y. Elyahu *et al.*, Aging promotes reorganization of the CD4 T cell landscape toward extreme regulatory and effector phenotypes. *Sci Adv* **5**, eaaw8330 (2019).
4. V. I. Korolchuk, S. Miwa, B. Carroll, T. von Zglinicki, Mitochondria in Cell Senescence: Is Mitophagy the Weakest Link? *EBioMedicine* **21**, 7-13 (2017).
5. N. Sun, R. J. Youle, T. Finkel, The Mitochondrial Basis of Aging. *Mol Cell* **61**, 654-666 (2016).
6. G. Desdin-Mico *et al.*, T cells with dysfunctional mitochondria induce multimorbidity and premature senescence. *Science* **368**, 1371-1376 (2020).
7. H. Oh *et al.*, An NF-kappaB Transcription-Factor-Dependent Lineage-Specific Transcriptional Program Promotes Regulatory T Cell Identity and Function. *Immunity* **47**, 450-465 e455 (2017).
8. Y. Grinberg-Bleyer *et al.*, NF-kappaB c-Rel Is Crucial for the Regulatory T Cell Immune Checkpoint in Cancer. *Cell* **170**, 1096-1108 e1013 (2017).
9. J. van der Veeken *et al.*, The Transcription Factor Foxp3 Shapes Regulatory T Cell Identity by Tuning the Activity of trans-Acting Intermediaries. *Immunity* **53**, 971-984 e975 (2020).
10. M. Pasparakis, P. Vandenabeele, Necroptosis and its role in inflammation. *Nature* **517**, 311-320 (2015).
11. D. E. Christofferson, J. Yuan, Necroptosis as an alternative form of programmed cell death. *Curr Opin Cell Biol* **22**, 263-268 (2010).
12. P. Bernardi, L. Scorrano, R. Colonna, V. Petronilli, F. Di Lisa, Mitochondria and cell death. Mechanistic aspects and methodological issues. *Eur J Biochem* **264**, 687-701 (1999).
13. S. Lee, K. Park, J. Kim, H. Min, R. H. Seong, Foxp3 expression in induced regulatory T cells is stabilized by C/EBP in inflammatory environments. *EMBO Rep* **19**, (2018).
14. S. Verdura *et al.*, Resveratrol targets PD-L1 glycosylation and dimerization to enhance antitumor T-cell immunity. *Aging (Albany NY)* **12**, 8-34 (2020).
15. M. Lagouge *et al.*, Resveratrol improves mitochondrial function and protects against metabolic disease by activating SIRT1 and PGC-1alpha. *Cell* **127**, 1109-1122 (2006).

16. Z. Fu *et al.*, Requirement of Mitochondrial Transcription Factor A in Tissue-Resident Regulatory T Cell Maintenance and Function. *Cell Rep* **28**, 159-171 e154 (2019).
17. N. M. Chapman *et al.*, mTOR coordinates transcriptional programs and mitochondrial metabolism of activated Treg subsets to protect tissue homeostasis. *Nat Commun* **9**, 2095 (2018).
18. P. V. S. Vasileiou *et al.*, Mitochondrial Homeostasis and Cellular Senescence. *Cells* **8**, (2019).
19. J. Zhu, W. E. Paul, Heterogeneity and plasticity of T helper cells. *Cell Res* **20**, 4-12 (2010).
20. S. A. McClymont *et al.*, Plasticity of human regulatory T cells in healthy subjects and patients with type 1 diabetes. *J Immunol* **186**, 3918-3926 (2011).
21. R. Mathur *et al.*, A mouse model of Salmonella typhi infection. *Cell* **151**, 590-602 (2012).
22. R. Mathur *et al.*, Induction of autophagy in Cx3cr1(+) mononuclear cells limits IL-23/IL-22 axis-mediated intestinal fibrosis. *Mucosal Immunol* **12**, 612-623 (2019).
23. S. G. Park *et al.*, T regulatory cells maintain intestinal homeostasis by suppressing gammadelta T cells. *Immunity* **33**, 791-803 (2010).
24. T. Stuart *et al.*, Comprehensive Integration of Single-Cell Data. *Cell* **177**, 1888-1902 e1821 (2019).
25. S. L. Wolock, R. Lopez, A. M. Klein, Scrublet: Computational Identification of Cell Doublets in Single-Cell Transcriptomic Data. *Cell Syst* **8**, 281-291 e289 (2019).
26. M. S. Kowalczyk *et al.*, Single-cell RNA-seq reveals changes in cell cycle and differentiation programs upon aging of hematopoietic stem cells. *Genome Res* **25**, 1860-1872 (2015).
27. C. Hafemeister, R. Satija, Normalization and variance stabilization of single-cell RNA-seq data using regularized negative binomial regression. *Genome Biol* **20**, 296 (2019).
28. G. La Manno *et al.*, RNA velocity of single cells. *Nature* **560**, 494-498 (2018).
29. V. Bergen, M. Lange, S. Peidli, F. A. Wolf, F. J. Theis, Generalizing RNA velocity to transient cell states through dynamical modeling. *Nat Biotechnol* **38**, 1408-1414 (2020).
30. B. Van de Sande *et al.*, A scalable SCENIC workflow for single-cell gene regulatory network analysis. *Nat Protoc* **15**, 2247-2276 (2020).
31. A. M. Bolger, M. Lohse, B. Usadel, Trimmomatic: a flexible trimmer for Illumina sequence data. *Bioinformatics* **30**, 2114-2120 (2014).
32. D. Kim, B. Langmead, S. L. Salzberg, HISAT: a fast spliced aligner with low memory requirements. *Nat Methods* **12**, 357-360 (2015).
33. Y. Liao, G. K. Smyth, W. Shi, featureCounts: an efficient general purpose program for assigning sequence reads to genomic features. *Bioinformatics* **30**, 923-930 (2014).
34. M. I. Love, W. Huber, S. Anders, Moderated estimation of fold change and dispersion for RNA-seq data with DESeq2. *Genome Biol* **15**, 550 (2014).

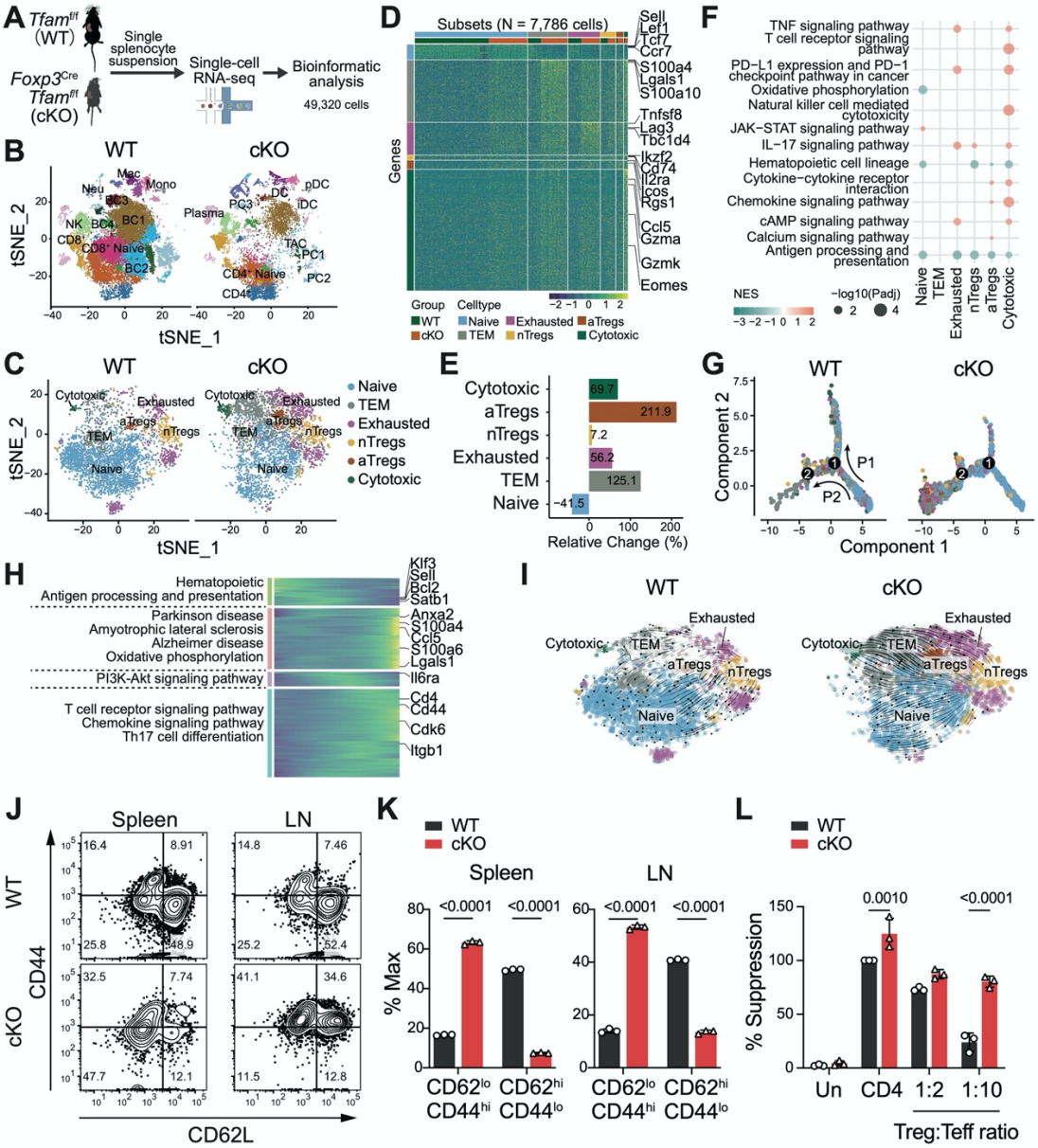

Figure 1: TFAM in FOXP3 Tregs role as a determinant of CD4-lineage distribution and to regulate immune-mediated aging. **A.** schematic representation of the scRNA sequence. **B.** t-SNE projection of 49,320 cells with 21 cell types (Erythroid cells were removed) were obtained from Foxp3^{Cre}Tfam$^{f/f}$ (cKO: 14,156) and controlled splenocyte Tfam$^{f/f}$ (WT: 35,164). Colors represent for different cell types. **C.** t-SNE projection of all 7,786 cells (WT: 4,133; cKO: 3,653) of CD4$^+$ T cells presenting six different CD4$^+$ T cells (Naïve, TEM, Exhausted, nTregs, aTregs and Cytotoxic cells). Colors indicate different cell types. **D.** Heatmap of gene expression profile across cells. All CD4$^+$ T cells were grouped by subset and groups (horizontal bars). Genes shown were up-regulated significantly [log2(fold change) > 0.25, adjusted P < 0.05] in at least one subset compared to all other cells. Genes were ordered by significance and associated with the subset with higher detection rates. **E.** Relative changes of six types of CD4$^+$ T cell between cKO and WT spleen. **F.** GSEA for KEGG pathways for CD4$^+$ T cells between cKO and WT. Color stands for the up-regulated (red) or down-regulated (blue) in cKO spleen. **G.** Pseudo time map of the CD4$^+$ T cells reflects the developing relationships and reveals potential paths of the CD4$^+$ T subtypes in WT and cKO. Each dot represents one cell and color stands for different cell type. **H.** Expression pattern for the expression of the 2,397 ordering genes. Cells were ordered in pseudotime; columns represent cells, rows representing genes were grouped based on similarity in gene expression, resulting in four clusters, with genes in clusters 1 expressed early in pseudotime, and genes in cluster 2 expressed late. KEGG enrichment analyses were performed for genes in each cluster, with selected significantly enriched pathways shown. **I.** Velocities derived from the dynamical model for CD4$^+$ T cells are visualized as streamlines in a t-SNE-based embedding. **J.** CD4$^+$CD44^{hi}CD62^{lo} CD4 effector and CD4$^+$CD44^{lo}CD62^{hi} CD4 naïve T cell from WT and cKO detected by FACS, and **K.** mean fluorescence intensity (MFI) plot from different organs. CD4$^+$ T effector T cell number greatly increased in lung, skin, and colon of the cKO mice compared to the WT mice. **L.** T cell suppression assay for CFSE labeled CD4$^+$ Tconv cells co-cultured with Tregs in indicated ratio for 60 hours in the presence of CD3/CD28 stimulated or non-stimulated Tconv cell CFSE proliferation detected by FACS Symphony, data analyzed by FlowJo, plotted as percent suppression.

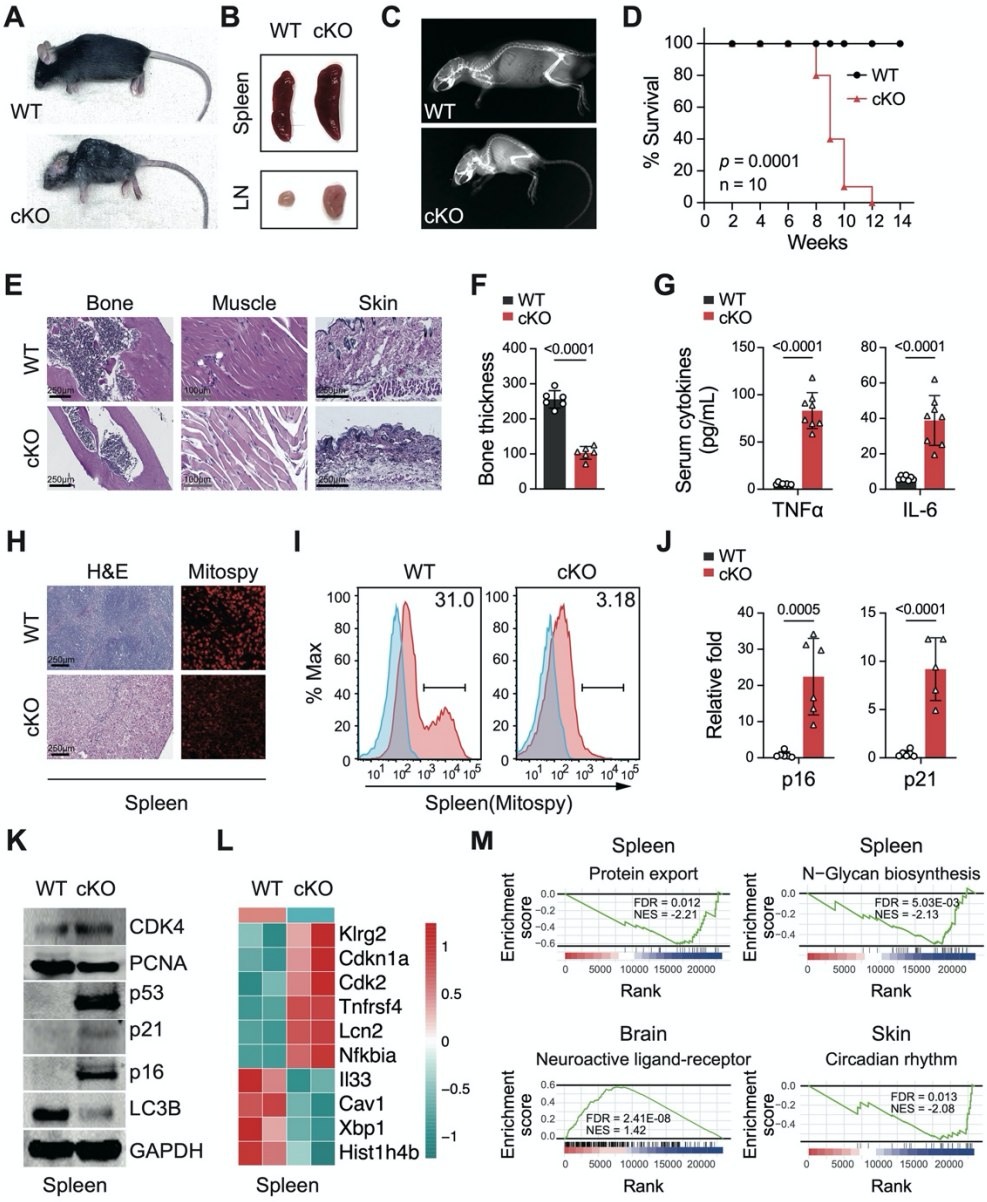

Figure 2: TFAM ablation exhibits systemic pathology and accelerates immune aging in Foxp3^{YFPCre}Tfam$^{f/f}$ mice.
A. Representative photograph from cKO mouse(right) exhibits deteriorated appearance compared to the same age (8week) and sex littermate WT mouse(left). **B.** Increased spleen and lymph node size in cKO mouse compared to WT mouse. **C.** cKO mouse(right) shows increased spine curvature compared to the same age (8week) and sex littermate WT mouse(left) showing by representative X Ray image. **D.** Kaplan Meir survival curve for WT (n=10; M/F) and cKO mice (n=10, M/F). **E.** Histology sections stained by H&E from bone, muscle and skin and images were taken by light microscope, and **F.** quantification of muscle and bone density plotted. **G.** Serum cytokines from for TNFα and IL6 were detected by Legend plex, and calculated values were plotted **H.** H&E and Mitospy staining in spleen section form cKO mouse compared to WT mouse. **I.** Mitospy staining from WT and cKO splenocytes, detected by FACS and plotted as a histogram. **J.** p16 and p21 aging marker from mouse spleen detected by quantitative PCR and plotted. **K.** Protein expression of aging markers including, CDK4, PCNA, p53, p21, p16, LC3B and GAPDH detected by western blot. **L.** Differential expression genes expression profiling between WT and cKO in the spleen. **M.** Bulk RNA Seq expression from cKO mice compared to the WT mouse showing reduced protein and N-Glycan biosynthesis pathways in spleen and reduced circadian rhythm in the skin, increased neuroactive ligand receptor signaling in the brain and of cKO mice.
Data represented as mean ± SEM t-test. $^{*}p < 0.05$, $^{**}p < 0.01$, and $^{***}p < 0.0001$, WT (n=5-10; M/F) and cKO mice (n=5-10, M/F).

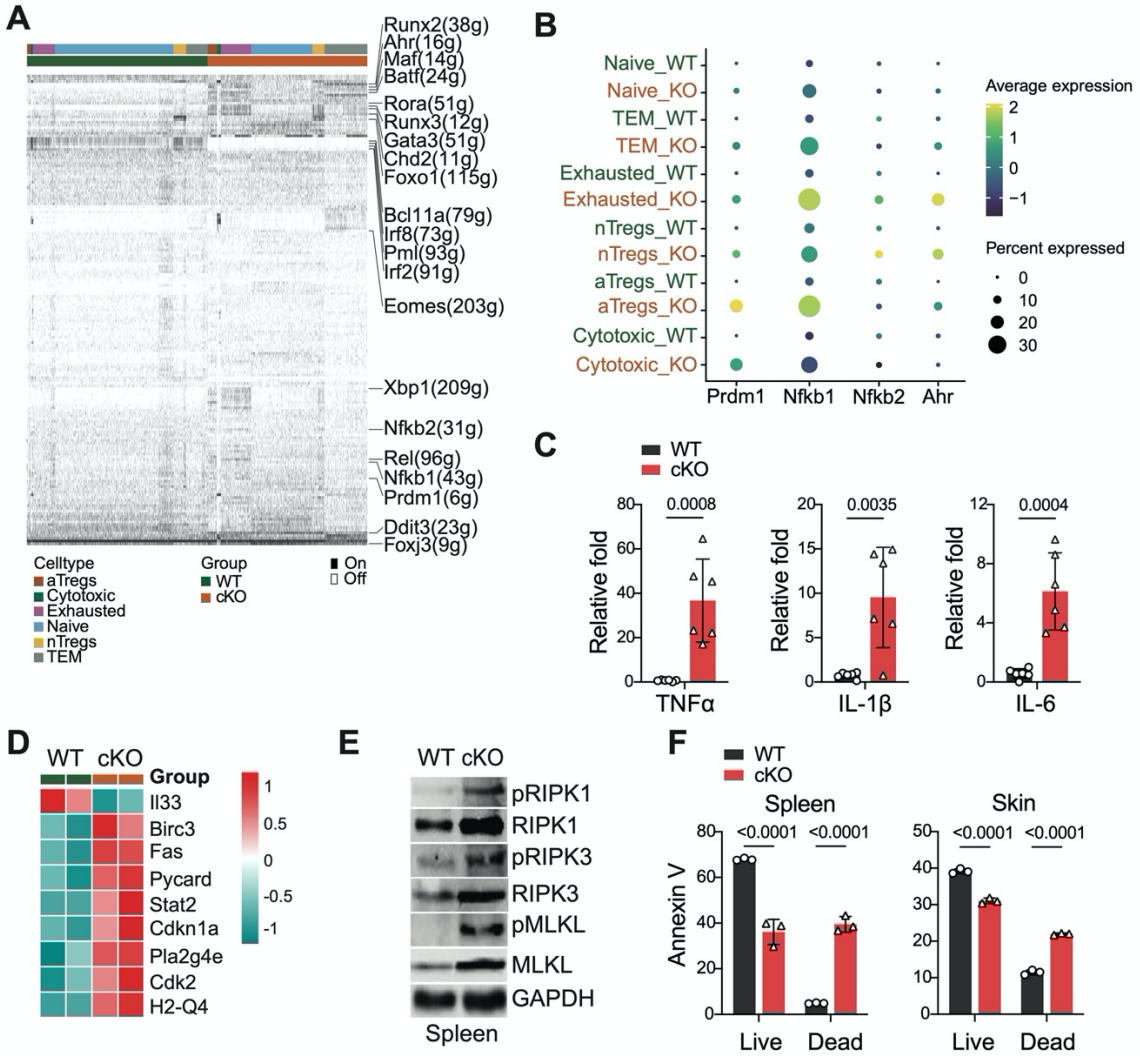

Figure 3. Predominance of inflammatory and cell death pathways in TFAM cKO mice

A. Heatmap of all CD4$^+$ T cells showing the high-confidence regulons among WT and cKO mice. "On" indicates active regulons; "Off" indicates inactive regulons. Active regulons per cell appear in black; the horizontal color bar indicates the subset associated with each cell and group. Numbers in parentheses represent the number of genes comprising the regulon. **B.** Dotplot showed the expression of *Prdm1*, *Nfkb1*, *Nfkb2* and *Ahr* between WT and cKO among all CD4$^+$ T cells. **C.** Inflammatory *TNF*α, *IL1*β, and *IL6* cytokines expression detected by qPCR from WT and cKO spleen. **D.** Heatmap showed the apoptosis and necroptosis expression profiling between WT and cKO in the spleen. **E.** Protein expression of TNF downstream pRIPK1/RIPK1, pRIPK3/RIPK3, pMLKL/MLKL and GAPDH as loading control detected by western blot. **F.** Annexin V staining for live and dead cell from spleen and skin detected by flowcytometry in WT and cKO mice.

Data represented as mean ± SEM t-test. $^*p < 0.05$, $^{**}p < 0.01$, and $^{***}p < 0.0001$, WT (n=5-10; M/F) and cKO mice (n=5-10, M/F).

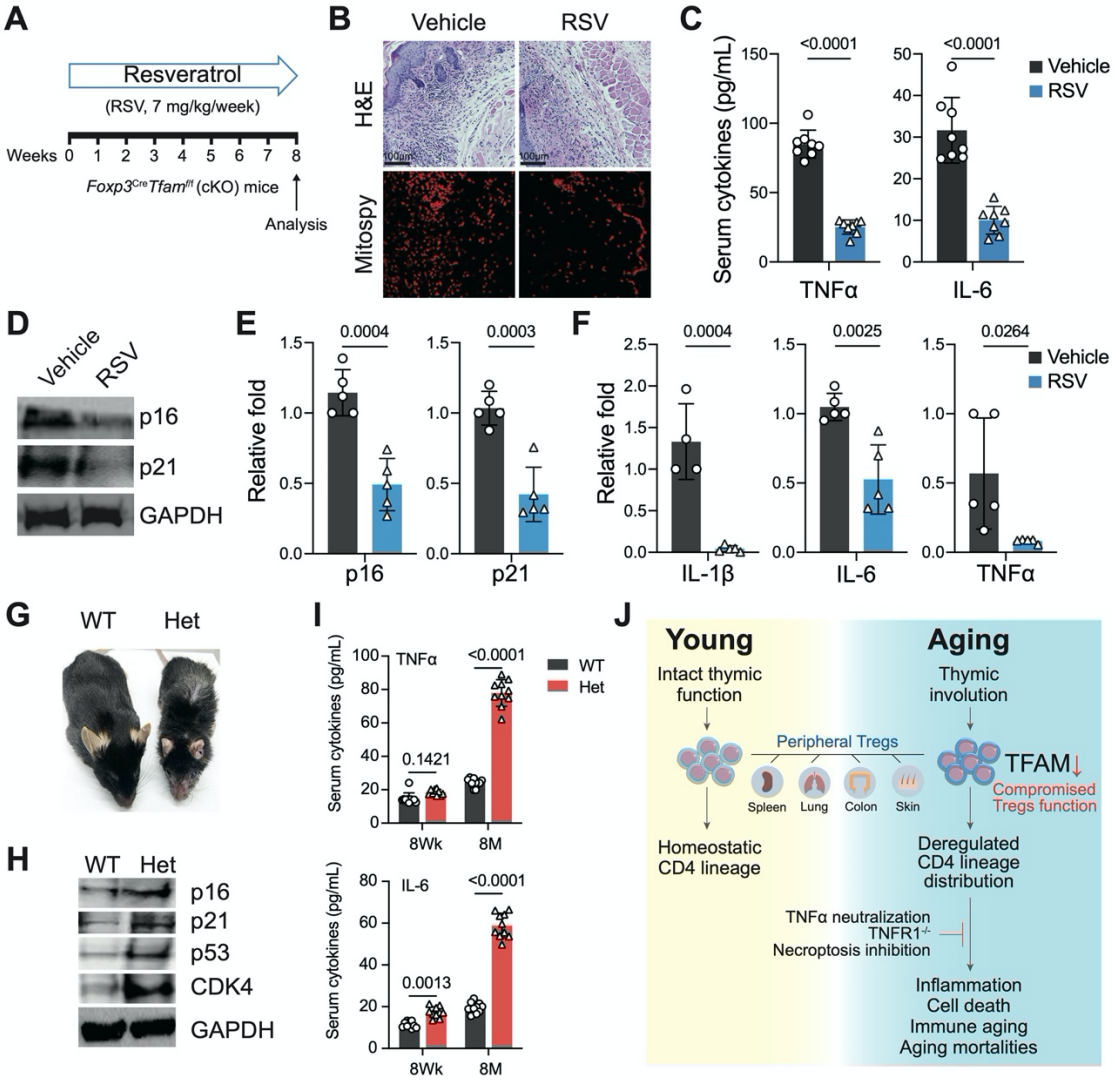

Figure 4. The restoration of TFAM function results to alleviate inflammation and aging pathologies.
A. Schematics for resveratrol (RSV) treatment for cKO mice. **B.** Skin histological sections stained for H&E and Mitospy from vehicle and resveratrol treated cKO mice. **C.** TNFα and IL6 serum cytokines from TFAM cKO mice**. D.** *p16* and *p21* expression detected by western blot, and **E.** qPCR from vehicle and resveratrol treated cKO mice. **F.** Proinflammatory *IL1β*, *Il6*, and *TNFα* cytokine expression detected by qPCR from vehicle and resveratrol treated cKO mice. **G.** Representative photograph from TFAM Het (Foxp3^{YFPCre}Tfam$^{f/+}$) mouse showing an aging appearance compared to the same age (8 months) and sex littermate control Tfam$^{f/f}$ mouse(left). **H.** Protein expression of aging markers including p16, p21, and GAPDH detected by western blot. **I.** TNFα and IL6 cytokine detected from serum from 8 week and 8 months of WT and cKO mice. **J.** Representative working model.
Data represented as mean ± SEM t-test. $^{*}p < 0.05$, $^{**}p < 0.01$, and $^{***}p < 0.0001$, WT (n=5-10; M/F) and cKO mice (n=5-10, M/F).

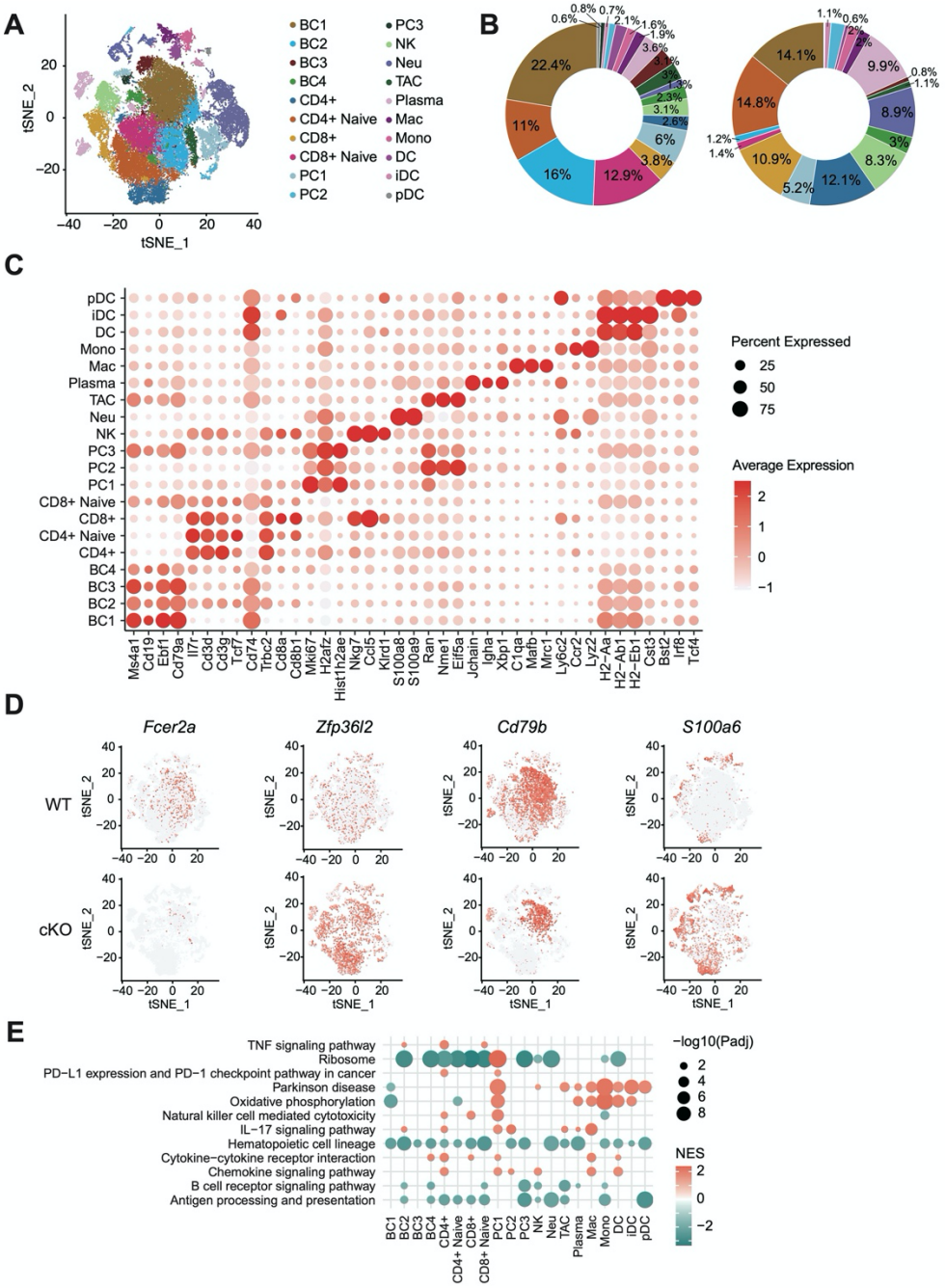

Supplementary Figure 1. Landscape of scRNA-seq analysis of WT and cKO spleen.
A. t-SNE projections of single-cell transcriptomes from WT and cKO mice before Erythroid cells were removed, annotated by cell type. Each dot denotes a distinct cell. **B.** Cell subset proportions for WT and cKO spleens. **C.** Dot plot of mean expression of canonical marker genes for 20 major lineages from tissues of each origin, as indicated. **D.** Expression of aged-related genes (*Fcer2a*, *Cd79b*, *Zfp36l2*, and *S100a6*) on Figure 1 t-SNE embedding. Each dot corresponds to a single cell. **E.** Gene Set Enrichment Analysis (GSEA) of KEGG pathways for all cell types between cKO and WT (Only age-related pathways are selected). Color stands for the up-regulated (red) or down-regulated (blue) in cKO spleen. Enriched terms were identified as significant at an adjusted P value ≤ 0.05.

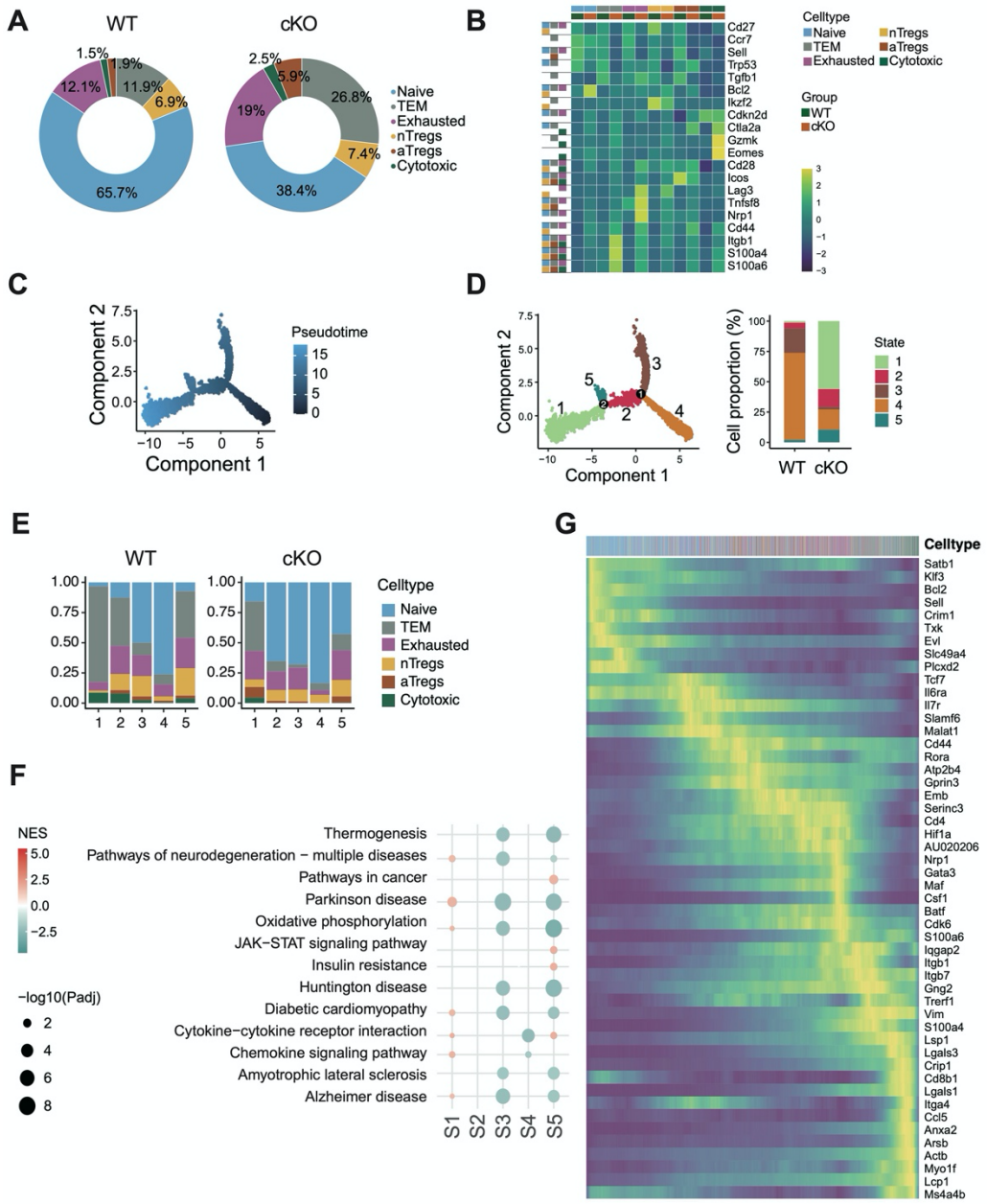

Supplementary Figure 2. scRNA-seq results show the cellular heterogeneity in CD4+ T cells.
A. Relative proportion of $CD4^+$ T cells among WT and cKO spleen, color stands for cell type. **B.** Heatmaps show the expression profile of age-related genes among all $CD4^+$ T cells. Only the significant differential expression genes between cKO and WT spleen in at least one of these six types of $CD4^+$ T cells were selected. **C.** Monocle 2 prediction of CD4+ T cell subsets developmental trajectory with pseudotime. Each dot represents a single cell. **D.** Relative proportion of $CD4^+$ T cells among different states of WT and cKO spleen, color stands for cell type. **E.** Differentiation trajectory generated with all $CD4^+$ T cells, each branch represents one cell state. (right). Barplots representing cell proportions in the five states of WT and cKO (left). Cells are colored according to five states, which partition the trajectory. **F.** Gene Set Enrichment Analysis (GSEA) of KEGG pathways for the five cell states. **G.** Gene expression dynamics resolved along latent time shows a clear cascade of transcription in the top 50 likelihood-ranked genes.

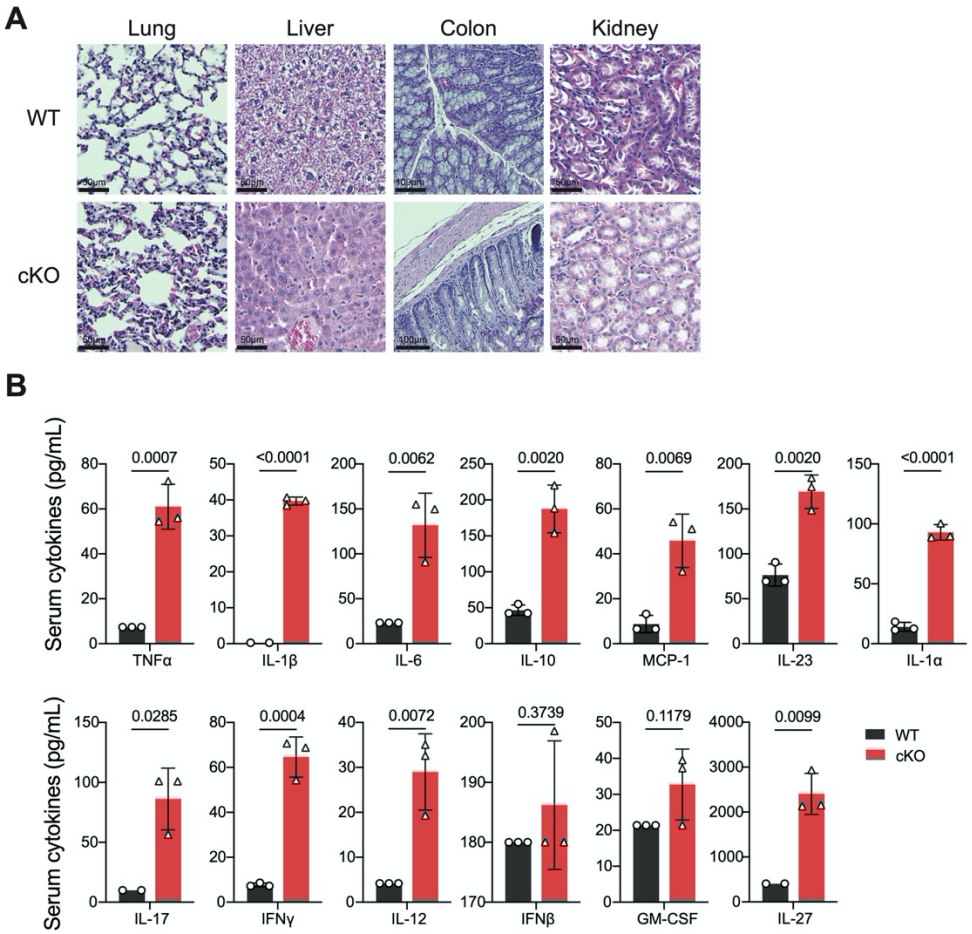

Supplementary Figure 3. Increased cell infiltration and inflammation in different organs in Foxp3 Tfam$^{f/f}$ mice.
A. Histology sections stained with H&E from lung, liver, colon, and kidney. **B.** Serum cytokines identified by Legend plex for TNFα, IL1β, IL6, IL10, MCP1, IL23, Il1α, IL17, IFNγ, and IL12, IFNβ, GM-CSF and IL27 with estimated values displayed.
Data represented as mean ± SEM t-test. $^{*}p < 0.05$, $^{**}p < 0.01$, and $^{***}p < 0.0001$, WT (n=5-10; M/F) and cKO mice (n=5-10, M/F).

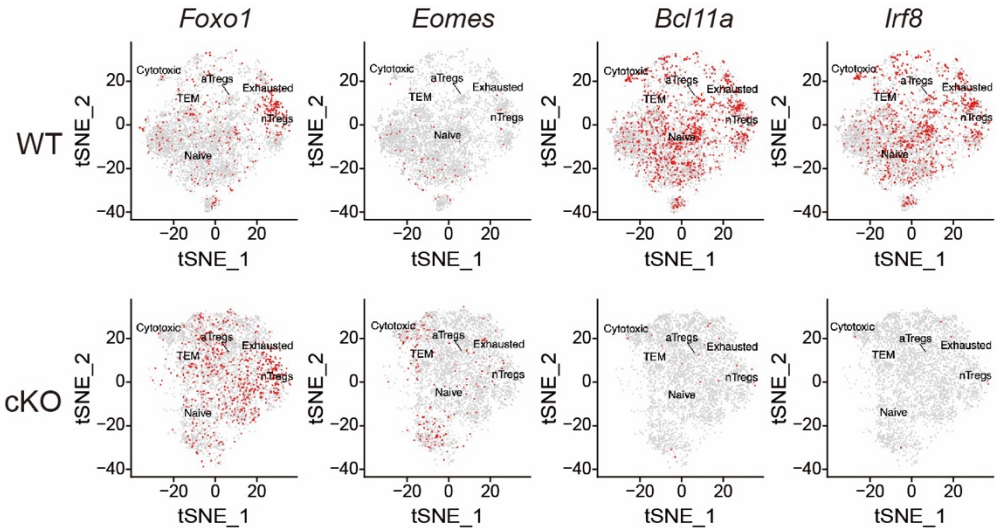

Supplementary Figure 4. t-SNE projection of average binary regulon activity of *Foxo1*, *Eomes*, *Bcl11a*, and *Irf8* that were cell type and group-specific in $CD4^+$ T cells.

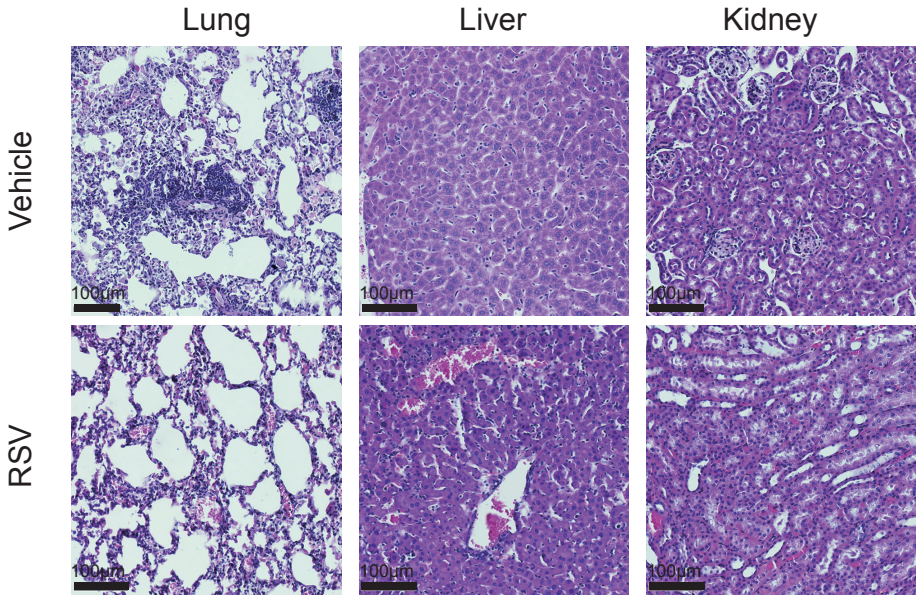

Supplementary Figure 5. H&E histology section for lung, liver, and kidney for RSV treated WT and cKO mice**.**